This is a repository copy of *Mapping of axial plastic zone for roller bearing overloads using neutron transmission imaging*.

Mapping of axial plastic zone for roller bearing overloads using neutron transmission imaging

A. Reid [a,*], I. Martinez [a], M. Marshall [a], T. Minniti [b], S. Kabra [b], W. Kockelmann [b], T. Connolley [c], M. Mostafavi [d]

[a] University of Sheffield, Dept. Mechanical Engineering, Sheffield S1 3JD, UK
[b] STFC-Rutherford Appleton Laboratory, ISIS Facility, Harwell OX11 0QX, UK
[c] Diamond Light Source Ltd., Harwell Science and Innovation Campus, Didcot, Oxfordshire OX11 0DE, UK
[d] University of Bristol, Dept. Mechanical Engineering, Bristol BS8 1TR, UK

HIGHLIGHTS

- A loading frame was designed to simulate bearing overloads on the ENGIN-X strain diffractometer at ISIS neutron source, UK.
- Neutron transmission imaging was used to map a Bragg edge fitting parameter, associated with material yielding.
- It was demonstrated that bearing overloads generate regions of subsurface plasticity in overloaded roller bearings.
- Subsurface deformation, observed during roller bearing overload events, appears to reduce the bearings life expectancy.

GRAPHICAL ABSTRACT
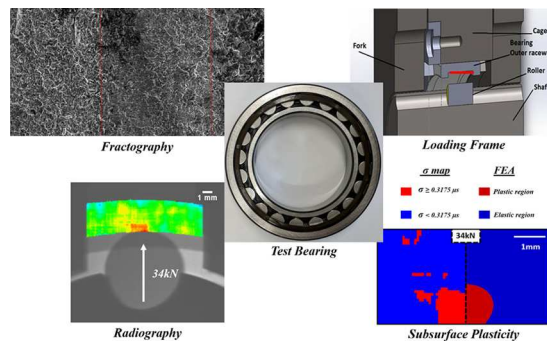
ABSTRACT

Premature failure of wind turbine gearbox bearings is an ongoing concern for industry, with sudden overload events potentially contributing towards raceway damage, significantly hindering performance. Subsurface stresses generated along a line contact cause material yielding, and a probable crack initiation site. Currently, the ability to study subsurface plastic zone evolution using non-destructive techniques is limited. Neutron Bragg edge imaging is a novel technique, allowing for two-dimensional mapping of the Bragg edge broadening parameter, indicative of bulk plastic deformation. An experiment on the ENGIN-X strain scanning instrument, at the ISIS neutron source, UK, was setup for Bragg edge transmission imaging, to measure the effect of in situ loading on the raceway of a bearing, scaled-down from a traditional wind turbine gearbox bearing. Results demonstrate a strong correlation between load and the Bragg edge width, and allow for future experimental development in studying, not only the effect of overloads on fatigue life, but also the use of neutron imaging for evaluating plastic deformation in engineering components.

1. Introduction

Wind turbine gearbox bearings, even after decades of engineering optimisation, are still considered to be the root-cause of many failures. Even with the presence of ISO gearbox design standards and specifications [1], bearings continue to fail significantly prematurely, when

compared to their design lifetimes [2]. Within the UK, 35.1% of claims processed from wind turbine operators were due to the deterioration of the gearbox [3]. The detrimental impact on installation and operating costs of wind turbines has directed research attention towards further understanding the causes of failure.

Cylindrical roller bearings, such as those found in a wind turbine gearbox, are generally designed to withstand heavy radial loads at moderate rotational speeds [4, 5]. Whilst there are various roller bearing failure mechanisms operating simultaneously, rolling contact fatigue (RCF) contributes substantially. RCF may occur in the subsurface, with many studies indicating cyclic subsurface shear stresses, combined with inherent defects, significantly contribute to damage in the static raceway [6–8].

Sudden torque spikes associated with transient conditions and inertial effects within the gearbox induce high large plastic strain in the subsurface of the static raceway [9]. Along with continued cyclic shear strains caused by RCF, failure within this region is inevitable. Subsurface yielding resulting from sudden overload events is a recognised cause of premature failure, with Hertzian contacts displaying greatest shear stresses in the subsurface [10]. Evaluating the evolution of subsurface plasticity for complex geometries, such as bearing contact sites, is yet to be fully evaluated with non-destructive techniques.

Laboratory destructive techniques such as scanning electron microscopy (SEM) and electron backscatter diffraction (EBSD) have been used to characterise the damage caused by sub-surface plasticity. It has been observed that subsurface plastic deformation damage in bearings are often associated with butterfly cracking at the white etch area (WEA) [11]. WEA is a region associated with nano-recrystallised carbide-free ferrite [12]. EBSD has been used to measure strain associated with fatigue cracks [13]. EBSD has also been successfully used to measure plastic strains in polycrystalline material [14], in combination with SEM. This technique uses the variation in crystal orientation in respect to a reference configuration, along with the analysis of local dislocation density distributions to provide accurate plastic strain measurements. It is however restricted to near surface measurements, typically to depths of 10–50 nm [15], meaning that 'in situ' bulk strain measurements are highly impractical.

It is now common practice to non-destructively measure elastic strain in materials using higher energy techniques, such as synchrotron X-ray [16–18]. X-ray diffraction application to quantify plastic strain is limited however [19]. In X-ray diffraction, lattice spacings for specific *hkl* planes (*hkl* being the miller indices [20]), represented as Bragg peaks are measured. The change in spacing is associated with elastic strain, calculated by measuring the shifts in these interplanar spacings [21]. Attempts have been made to measure plastic strain in diffraction methods by correlating the plastic deformation with the Bragg peak width [22]. Plastically deformed materials exhibit diffraction peak broadening, with this effect becoming more prominent as levels of plasticity increase [22]. Full width at half maximum (FWHM) of the diffraction peaks are often used as measure of plastic strain [23]. However, the ability to use this peak broadening effect to quantify plastic strain is limited since other mechanisms such as stacking faults and/or planar defects also contribute towards peak broadening [24]. Other external factors contributing to peak broadening, impacting the reliability of measurements, include instrumental effects, notably when comparable with dislocation density being correlated with plastic deformation [25].

Similar to X-ray diffraction, neutron strain diffraction has developed significantly in recent decades [26], with advantages and disadvantages over synchrotron X-ray diffraction strain measurement techniques. Neutrons are capable of penetrating greater depths in typical engineering components, such as metals and metal matrix composites [27, 28]. Neutron scattering behaviour permits the investigation of materials possessing low atomic masses, with this benefit being utilised, for example, to directly study hydrogen trapping sites during the hydrogen embrittlement of bearing steel [29]. On the other hand, synchrotron

X-rays provide enhanced spatial resolution and incident flux, compared with neutron techniques, greatly reducing the time required for data acquisition [21]. Bragg peak broadening investigations are also used in neutron diffraction [22, 30]. For example Huang et al. observed increases in FWHM as a result of increased dislocation density, associated with gross plastic deformation during an in situ tensile loading experiment using annealed nickel alloy [31].

In this paper, Bragg edge transmission imaging has been used to identify the presence of plastic strain, through observation of edge broadening. This neutron imaging technique provided the opportunity to measure and generate two-dimensional maps of averaged elastic strains and observe plastic zone evolution in bulk materials with high spatial resolution [32]. FEA was used to compare simulation with experimental plastic zone evolution, allowing for result validation and a reliable method for predicting changes in subsurface plasticity.

2. Experimental design

2.1. Neutron Bragg edge transmission imaging

Neutron Bragg edge transmission imaging, or energy-dispersive neutron imaging, is a less conventional neutron scattering technique. As with the more established time of flight (TOF) and monochromatic neutron diffraction methods, it can be used to obtain strain information from polycrystalline materials non-destructively. Neutron transmission spectra contain sudden increases of intensity above the critical wavelength at which Bragg's law is no longer satisfied, and diffraction no longer occurs for a given family of (*hkl*) lattice planes [33]. These points of sudden change in intensity, known as Bragg edges, occur at wavelengths corresponding to $2d_{hkl}$ (twice the lattice spacing). An exaggerated comparison between a Bragg edge from an unloaded and loaded sample can be seen in Fig. 1. The shift in edge position, λ, is associated with elastic strain, whilst the broadening effect, σ, is indicative of plastic deformation.

Measuring strain from shifts in Bragg edges is analogous to more common strain measurements from diffracted Bragg peaks. However, whilst conventional neutron diffraction is a point measurement technique, energy-dispersive neutron imaging allows for the generation of strain maps with spatial resolutions dependent on the individual pixel size of the detector [34]. Due to the increased neutron intensity measured in transmission, compared to that of a diffracted Bragg angle, data acquisition times for Bragg edge transmission imaging are significantly shorter than that required for neutron diffraction. Using neutron diffraction to generate a strain map of the same dimensions as a transmission scan region of interest, multiple individual point scans would need to be acquired. Depending on the diffraction gauge volume and number of point scans this could take several hours [35]. Neutron time

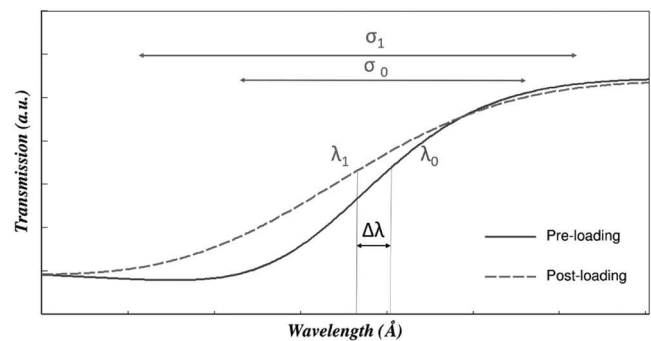**Fig. 1.** Comparison of Bragg edge taken from an unloaded and loaded sample, exaggerated to distinctly demonstrate the shift in edge position, λ, resulting from elastic strain, and edge broadening, σ, caused by plastic deformation.

of flight information is used to calculate wavelength with the equation:

$$\lambda_{hkl} = \frac{h t_{hkl}}{mL} \tag{1}$$

where λ_{hkl} is the neutron wavelength, h is Planck's constant, t_{hkl} is the neutron time of flight, m is the neutron mass, and L is the flight path from source to camera (neutron detector). The wavelength can then be correlated with the interplanar spacing d_{hkl}.

$$\lambda_{hkl} = 2 d_{hkl} \sin\theta \tag{2}$$

where λ_{hkl} is the wavelength at which {hkl} plane diffracts the neutron beam, d_{hkl} is the lattice spacing of the {hkl} plane. θ is the angle between the angle between the incident and the diffracted beam. In the case of neutron transmission, $2\theta = \pi$.

The average strain component in the beam direction may be calculated using the following definition of strain:

$$\epsilon = \frac{d_{hkl} - d_{hkl}^0}{d_{hkl}^0} \tag{3}$$

where d_{hkl}^0 is the interplanar spacing of the unstrained material. The strain accuracy of the method has been previously estimated as $\Delta\epsilon \approx 10^{-5}$ [36].

In a neutron Bragg edge transmission experiment, if counting times are long enough to gather data with sufficient statistics, the shape of the edges may be fitted using an analytical function [36]:

$$B(d_{hkl}, t) = \frac{1}{2}\left[\text{erfc}\left(-\frac{t - t_{hkl}}{\sqrt{2}\sigma}\right) - \exp\left(-\frac{t - t_{hkl}}{\tau} + \frac{\sigma^2}{2\tau^2}\right) \text{erfc}\left(-\frac{t - t_{hkl}}{\sqrt{2}\sigma} + \frac{\sigma}{\tau}\right) \right] \tag{4}$$

In which t is time, t_{hkl} is the time of flight associated with {hkl} plane, τ is a constant associated with the instrumental pulse width (pre-determined experimentally [36]), and σ defines the width of the Bragg edge. The σ parameter is increased by the presence of higher intragranular strain caused by dislocations, and fluctuating intergranular strain within a specific region [37], analogous to FHWM in a diffraction peak. As Bragg edge broadening, and increases in the σ parameter, are indicative of plastic deformation, experimental results focus on this relationship. The ability to map this broadening parameter offers the unique opportunity to qualitatively image the evolution of subsurface yielding in an overloaded roller bearing.

2.2. Test bearing

Wind turbine gearbox bearings are large components, unsuitable for neutron strain measurement techniques due to their high attenuation. A SKF, NU1010 ECP bearing was used in this research as it provides the opportunity to scale-down the sample size whist maintaining the contact conditions experienced in a wind turbine gearbox bearing. It was ensured that the selected sample bearing has the same average contact pressure through the contact area as the wind turbine bearing. The selected bearing has an outer diameter of 80 mm and bore diameter of 50 mm, with a thickness of 16 mm (along x direction – see Fig. 2) being of notable importance for this experiment, as this allows sufficient neutron penetration within the neutron wavelength range of interest (0.5–6 Å). Material properties for AISI 52100 bearing steel can be found in Table 1, whilst chemical composition is detailed in Table 2.

Experimental work using the same bearing has demonstrated that there is reasonable agreement between the stress measured experimentally by X-ray diffraction and that predicted by Hertzian contact mechanics [40]. Therefore, the elastic limit load of the bearing can be calculated by using theoretical Hertzian equations. The elastic limit load is based on the following rearrangement of Hertzian contact equation, assuming that the bearing elastic limit load is reached once the
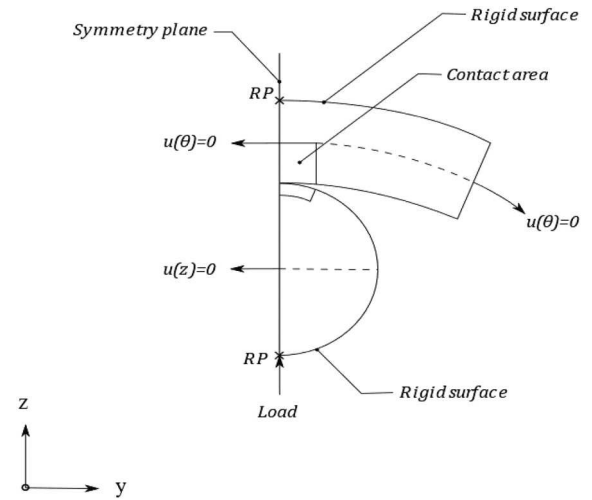

Fig. 2. Finite element model boundary conditions.

maximum von-Mises stress in the contact stress field reaches the material's yield stress.

$$F^Y = \frac{L \pi R^*}{E^*} \left(p^Y\right)^2 \tag{5}$$

$$p^Y = 1.67\sigma_Y \tag{6}$$

where p^Y, F^Y, L, R^* and E^* are the limit contact pressure, limit load, line contact length, equivalent radius, and equivalent Young's Modulus, respectively. σ_Y is material's yield stress. The equivalent Young's Modulus and the equivalent radius are calculated as:

$$E^* = \frac{2(1 - \nu^2)}{E} \tag{7}$$

$$R^* = \frac{1}{R_1} + \frac{1}{R_2} \tag{8}$$

To assess the effects of plastic overload on the life of the selected bearing, its life in normal conditions is to be calculated and compared with the overloaded reduced life measured experimentally. As the bearing life expectancy is largely statistical, it is standard practice to use the basic rating life, L_{10}, defined as the length of time in which 10% of bearings fail, stated in millions of cycles [41]. Basic rating life is calculated using the following equation [42]:

$$L_{10} = \left(\frac{C}{P}\right)^p$$

where C is the bearing dynamic load rating, P is the applied pressure and p is the load-life exponent (10/3 for roller bearings [42]). Adjustment factors may be used to predict life times with varying probabilities of failure [43], for example to calculate the expected time for 50% (L_{50}) or 90% (L_{90}) of bearings to fail.

Table 1
AISI 52100 properties [38].

Property	Symbol	Value
Density [kg/m^3]	ρ	7827
Young's Modulus [GPa]	E	201.33
Poisson's ratio	ν	0.3
Yield stress [MPa]	σ_Y	1410.17

Table 2
AISI 52100 chemical composition [39].

C	Mn	Si	Cr	Cu	S
0.95–1.10	0.20–0.50	≤0.35	1.30–1.60	≤0.025	≤0.025

Table 3
Contact pressure and load yield limits.

	FE model	Theoretical prediction	Absolute error (%)
p^Y [MPa]	2894.92	2805.6	3.18
F^Y [N]	9894.92	9285	3.90

2.3. Finite element analysis

It was critical to have an estimation of the bearing sub-surface plastic zone size as a function of applied load before the experiment. This is to determine an appropriate load, whereby the plastic zone can be identified using a neutron Bragg edge imaging detector with certain pixel size. A three dimensional finite element model was developed using ABAQUS version 6.14-2 [44] to estimate subsurface plastic zone evolution in the outer raceway. Schematic of the model can be seen in Fig. 2. The raceway and the rolling elements were modelled using quadratic elements (C3D20R). Deformation on the rest of the component, i.e. the case of the shaft and the rig's cage, was ignored by modelling it as a rigid body; bilinear rigid quadrilateral elements (R3D4) were used. As the region of interest (i.e. the outer raceway area close to the raceway-roller contact site) has high stress gradient profiles, a mesh refinement was performed in that zone. The contact area at the outer raceway was modelled using a mesh size of 0.02 × 0.02 mm, the elements in the contact area (indicated in Fig. 2) on the roller bearing were doubled in size, where its corresponding contact surface was defined as a master surface to prevent penetrations on the roller contact surface. This assumption was made as the roller surfaces are normally harder than the surface on outer raceway. The contact interaction was assumed to be frictionless for all the contact interactions in the model, also the contact between the roller and the outer raceway was modelled as a line contact, no effects on logarithmic profile were included. Assuming symmetry in the *z*-axis and *θ*-axis, a quarter of the bearing was modelled.

The model simulates the elastic-plastic behaviour of overloading, where initial yielding is governed by the distortion energy hypothesis (i.e. von-Mises stress). An isotropic hardening rule was used in the FE model derived from the stress-strain curve for AISI 52100 [45]. The model was solved in quasi-static conditions. Density values should be included in the analysis even though the inertial effects are going to be neglected, solving convergence issues during contact initiation between bodies in load-controlled problems. The active yielding zone, defined as the region where the material von Mises stress reached the materials yield stress, was of most importance for this analysis. The elements in the model where this condition is reached are flagged and their volume was added together by an in-house MATLAB code. Fig. 3 demonstrates the evolution of the expected plastic area from initiation at 10.3 kN to 34 kN, where plasticity has propagated to the raceway surface. For validation, the limit load of contact pressure of elastic limit load calculated from Hertzian contact stress theory was compared with that
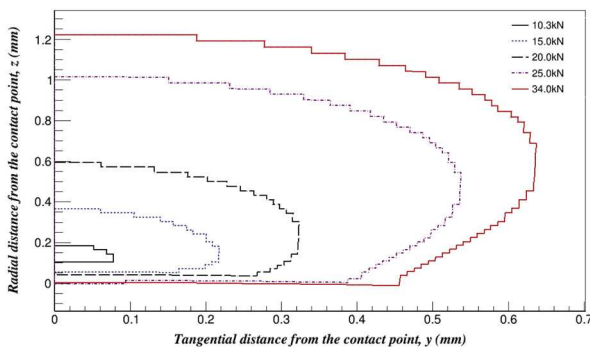
estimated by the finite element model. The results, reported in Table 3 shows excellent agreement validating the model.

3. Experiments and results

3.1. Bearing fatigue

To study the influence of overload events on the bearing life, a fixed raceway loading frame (FRLF) was designed to recreate an overload event within an isolated outer raceway, using a single rolling element. Fatigue tests were completed offline at University of Sheffield, UK, as neutrons were only required for the static overload experiment. The FRLF was mounted in an ESH servo hydraulic dynamic test machine (capacity 150 kN) with a Moog closed loop controller. Fig. 4 shows the setup of the overload experiment and details of the designed overloading frame. The test frame allowed static overloads to be applied on the bearing in displacement control at a rate of 0.2 mm/min and fatigue loads to be applied at 15 Hz.

The most extreme loading condition where yielding reaches the raceway surface, as shown by FE simulation (see Section 2.3), was overloading at $p^{overload} = 34$ kN. A static overload at 34 kN was followed by a fatigue load of $p^{max} = 10$ kN (maximum load below initiation of subsurface yielding, according to FE) and $p^{min} = 100$N. Sinusoidal loading was applied on the sample. The R ratio (p^{min}/p^{max}) of 0.001 intended to recreate the effect of roller passage, imitating pressure being removed from the raceway without repeated impact. After 5 million cycles (equivalent of approximately 2.78×10^5 revolutions), a well-defined crack was observed propagating axially along the line contact position. This signifies an approximated 64% reduction in the dynamic load rating, as a result of damage induced by the overload.

Fig. 5 shows the fracture surface of the bearing midway through its width (xz-plane) taken by an optical microscope with 20× magnification. The theoretical variation of the shear stress radially through the thickness of the bearing is included in this image with the point of maximum shear stress also being indicated. It can be seen that a white etching area (WEA) is present at depths between roughly 300 μm and 450 μm. A SEM image of this area is shown in Fig. 6, which shows a transition between the regions of highest shear stress caused by overload and the fatigue cracking region. The smoother surface, in the overload effected zone, is characteristic of ductile fatigue, whilst the region closest to the surface is rougher with spherical voids visible, indicative of ductile fracture. This suggests that subsurface fatigue crack growth became sufficiently high enough that the bearing lost its load-bearing capacity. It has been documented that higher than average carbon content in roller bearings, may give rise to WEA, increasing material hardness and providing initiation sites for fatigue cracking [12, 46]. This experiment confirmed the significant effect that an overload of 34 kN has on the reduction in life of the selected bearing. The shape and magnitude of the plastic zone was then investigated in depth using neutron transmission Bragg edge imaging.

3.2. Bragg edge imaging

This experiment was conducted on the ENGIN-X instrument at the ISIS pulsed neutron spallation source, located at the Rutherford Appleton Laboratory, UK. The FLRF was mounted on a 50 kN hydraulic Instron load frame, to overload an outer raceway using a single rolling element in situ (as in Section 3.1).
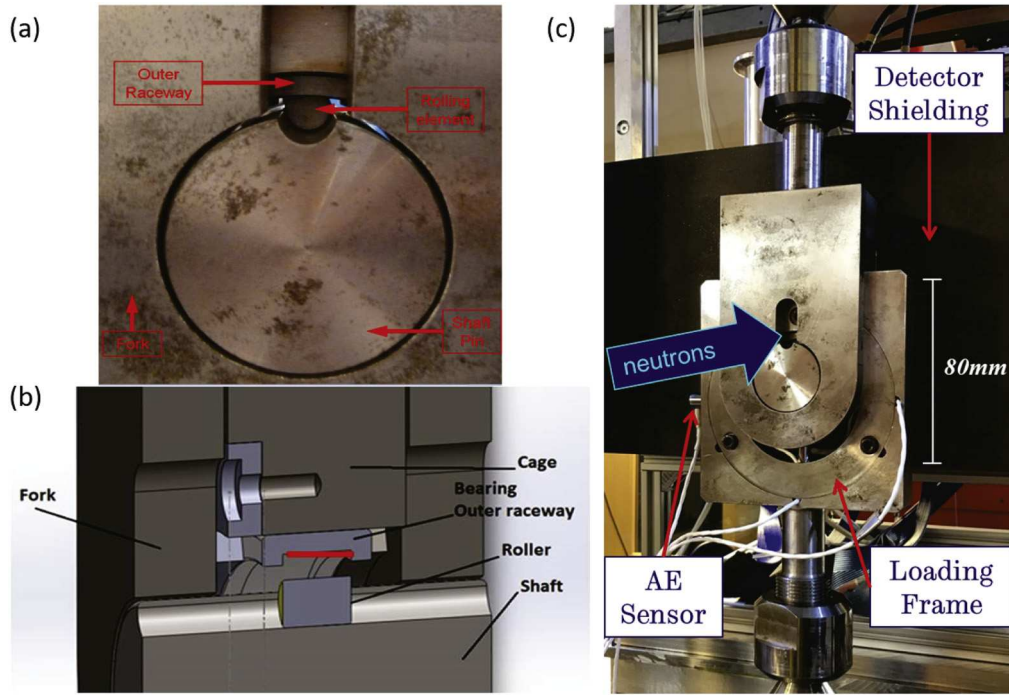

Fig. 3. Subsurface plastic zone as predicted FEA, from initiation (10.3 kN) to the load at which yielding reaches the raceway surface (34 kN).

Fig. 4. (a) Roller bearing and FLRF assembly. (b) CAD cross-section of the assembled FRLF visualising contact site (red line). (c) Experimental setup on ENGIN-X instrument, with MCP detector. (For interpretation of the references to color in this figure legend, the reader is referred to the web version of this article.)

Bragg edge neutron transmission imaging was undertaken using a TOF neutron camera, based on a microchannel plate (MCP) detector, designed by Nova Scientific and University of California at Berkley, for the IMAT imaging beamline at ISIS neutron source [32] [47]. The MCP consists of a 2×2 array of Timepix readout application specific integrated circuits (ASICS), with a total field of view of 28×28 mm^2 (512×512 pixels with individual pixel sizes of 55×55 μm^2) [48]. Within a pixel, a detected neutron generates an electron avalanche which is registered by the ASIC (CMOS) readout chip, whilst the neutron arrival time is also registered. For this experiment, a time resolution of 4.48 μs was set. The MCP has a detection efficiency of approximately 50% for neutron energy ranges relevant for to this study [49]. Details of the detector and its specifications can be found elsewhere [48, 50].

The MCP was positioned using a specially designed mounting arrangement, unique for this experiment (see Fig. 4c). Due to the non-uniform divergent nature of the neutron beam, it is preferable to minimise the distance between the sample and the detector in an imaging experiment. The camera was positioned at 48 mm from the furthest edge of the bearing raceway, as the FRLF geometry restricted the minimum distance. The scans were taken whilst the sample was held at any specified load, with the Instron in displacement control. The measured range of neutron time of flights for each scan was 18 ms to 55.7 ms.

ENGIN-X beamline is a strain diffractometer, and therefore not optimised for imaging experiments. Although flux on ENGIN-X is significantly lower than a dedicated imaging beamline, such as IMAT, ENGIN-
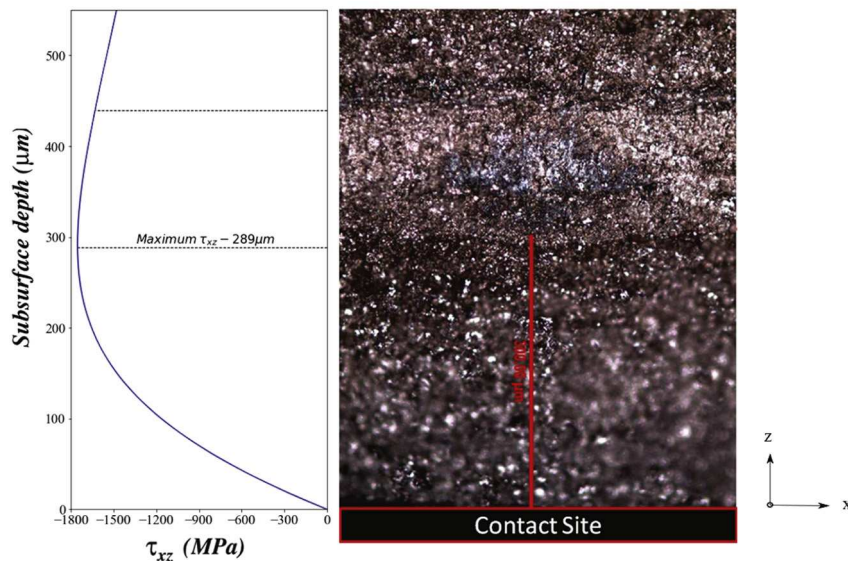

Fig. 5. Optical microscope image of the fracture surface under 20× magnification, with graphical representation of the subsurface shear stress shear stress at 34 kN, calculated using Hertzian contact mechanics.
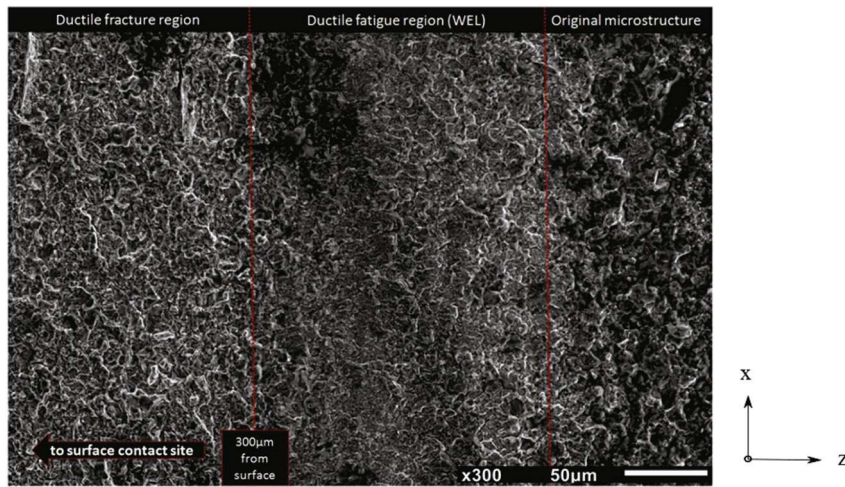
Fig. 6. SEM image (300× magnification) of the transition between the region of highest shear during fatigue loading, the white etching layer produce in the region of maximum shear from overloading, and the coarse pearlitic microstructure present in the unaffected zone.

X has the 2nd best resolution of any neutron beamline at ISIS. ENGIN-X was chosen for this experiment as it does provide the opportunity to carry out in situ testing using a 50 kN hydraulic loading frame. Material thickness will also influence the necessary scan times, with an optimum being found where the thickness allows for averaging over significant grain numbers without being overly attenuating. After trial experiments, it was concluded that the sample of 16 mm thickness required scan times of 2 h. This provides sufficient statistics for Bragg edge analysis, and completion of scans at several different loads within the allocated timeframe.

As each individual pixel records a separate transmission spectrum, any non-uniformity in the beam or variations in pixel response need to be accounted for. A flat field scan, where no sample is mounted, is used to normalise these neutron beam and detector effects. Flat field scans were taken prior to mounting and after removing the sample to improve statistics. Bragg edge transmission images were then taken at 0.4 (reference), 10 (elastic limit), 15, 25, and 34 (plasticity reaching surface) kN.

Bragg Edge Analysis for Transmission and Imaging Experiment (BE-ATRIX) software, was used to analyse the data recorded in this experiment, through the fitting procedure described by Santisteban et al. [36] to extract the individual fitting parameters for a specified edge [51]. A pixel situated in a region away from the contact site at an applied load of 400 N was chosen to measure the position of the stress-free Bragg edge associated with {110} plane and A Bragg edge position of 4.06510 Å, corresponding to $d_{hkl}^0 = 2.03255$Å was measured. This method for acquiring a stress-free measurement was chosen because the focus of this study is on Bragg edge broadening and elastic residual strain measurement was not a priority. Residual stress experiments require a highly accurate stress-free, or d_0, value [52] which requires non-negligible acquisition time. It was decided to spend more time acquiring data related to material yielding and use a far-field stress-free area of the sample whilst unloaded as a representative of a stress-free lattice spacing. BEATRIX software accounts for variation of Bragg edge position in calculating broadening, therefore, the lack of an exact stress-free Bragg edge position does not reduce the accuracy of broadening measurement. An example of the transmission spectra at 400 N load is given in Fig. 7, along with a BEATRIX fitted {110} Bragg edge with statistics corresponding to 31 × 31 pixel spatial binning.

The software uses the flat-field scan for normalisation and accounts for detector deadtime by means of an event overlap correction algorithm [53], outputting two-dimensional maps with pixel size spatial resolution for each individual fitting parameter, along with a map of strain. Parameters extracted using this technique are averaged through the thickness

of the sample, giving the averaged axial (ε_{xx}) strain (see Fig. 8 for coordinate system). Low signal-to-noise ratio's (SNR) within each individual pixel required spatial binning to gather sufficient data statistics for fitting edges with the required precision, visualised as a smoothing effect in the two-dimensional maps. Spatial binning of 31 × 31 pixels was used in the analysis for this experiment to improve counting statistics. The analysis is completed pixel by pixel, whilst recursively running an average mask of 31 × 31 neighbouring pixels, centred to that specific pixel under analysis, to ensure the statistics are sufficient to fit the Bragg edges [54].

The *bcc* (110) lattice plane was used to calculate strain as it has significantly greater intensity than the other available edges. The aim of this research was to evaluate Bragg edge broadening effects, which can be observed with greater confidence in edges of largest intensity. For *bcc* crystal structures the (211) lattice planes exhibit the most
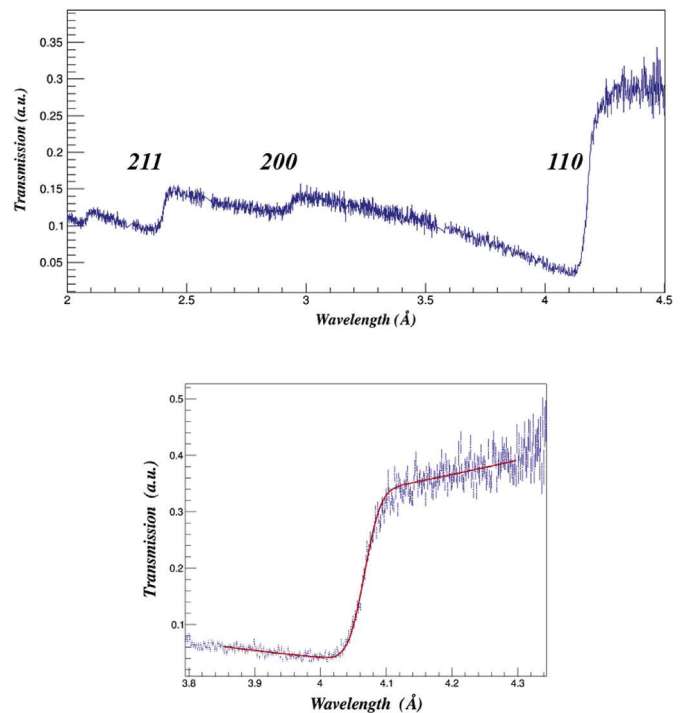

Fig. 7. Top: Neutron transmission spectrum through a bainitic SKF NU1010 ECP bearing outer raceway indicating Bragg edges associated with {110}, {200}, and {211}. Bottom: BEATRIX fit for a {110} edge using 31 × 31 pixel spatial binning statistics.
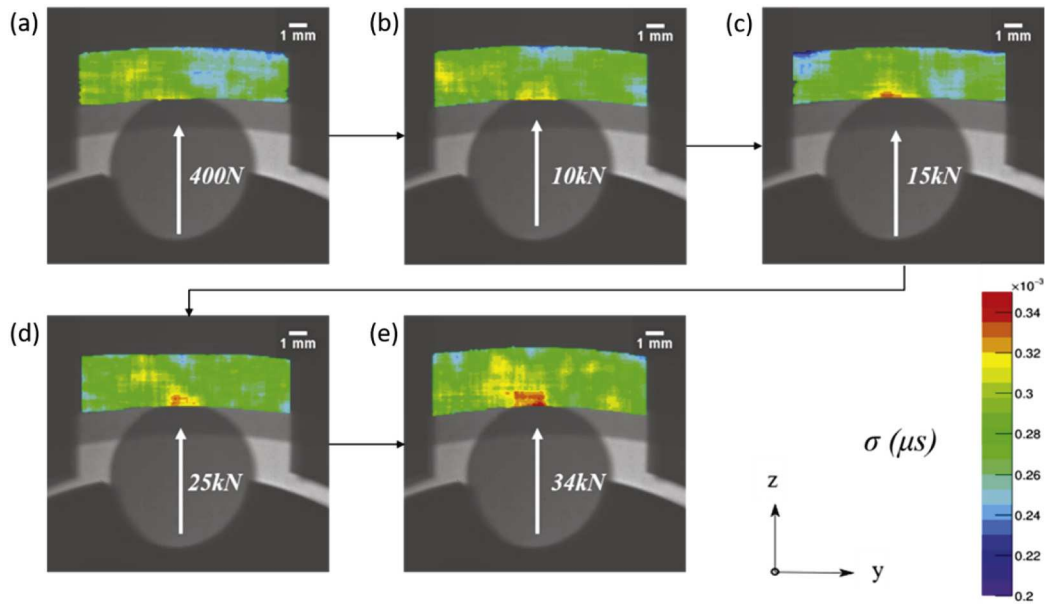
Fig. 8. 2D maps of the Bragg edge broadening parameter, σ, at various loads: (a) 0.4 kN (b) 10 kN (c) 15 kN (d) 25 kN (e) 34 kN.

favourable relationship with the macroscopic strain, yet the 110 Bragg edge suitably demonstrates the bulk elastic response [55]. In this study, elastic strain was not a primary focus, as the aim was to generate the shape of the plastic area. Material yielding generates substantial intergranular residual stress, therefore reducing the accuracy in elastic strain measurements when compared to the macroscopic applied stress field [56, 57].

Two-dimensional maps of Bragg edge broadening, quantified by σ in BEATRIX, were generated for two loads prior to yielding and three loads post plastic initiation, according to FEA. Fig. 8 displays the maps of the σ parameter, showing clear increases in the contact region as a function of increased load, indicative of subsurface yielding. Once 10 kN elastic limit is exceeded, the contact region demonstrates greater broadening, with this evolving until 34 kN load is reached. Due to the complexity of the mechanisms involved with plastic deformation, quantitative analysis of plastic strains is not yet possible using this technique. However, when comparing the increase of σ radially from the contact site, the greatest fluctuations post-yielding occur in the subsurface. Fig. 9

displays increases in the subsurface line profile extracted by the σ parameter maps, relative to the 400 N load, with values averaged across the Hertzian half contact width, 400 μm, corresponding to 7 pixels (385 μm). The cause of unexpected subsurface fluctuations in σ can only be speculated at this current time. For instance, bearing manufacturing and post-manufacturing treatment, such as shot peening may well cause variations in microstructure, resulting in differing response to load at different subsurface depths.

4. Discussion

4.1. Bragg edge imaging

Onset of yielding above 10 kN inherently makes measured elastic strain difficult to compare with FEA accurately, as plastic deformation generates substantial intergranular residual stress. Averaging through 16 mm of steel with such significant presence of plastic deformation would not allow for accurate elastic strain comparisons. Nevertheless,
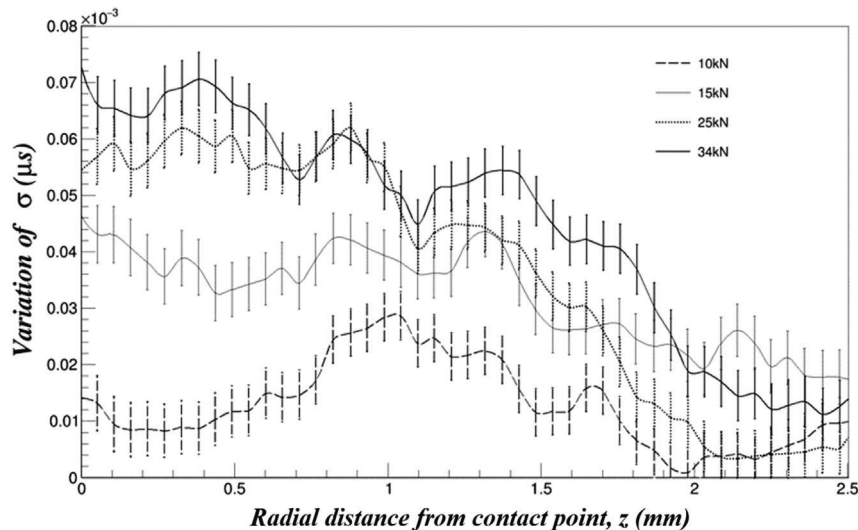

Fig. 9. Increase in sigma value from the contact site into the subsurface for several each loads, relative to the reference 400 N load.
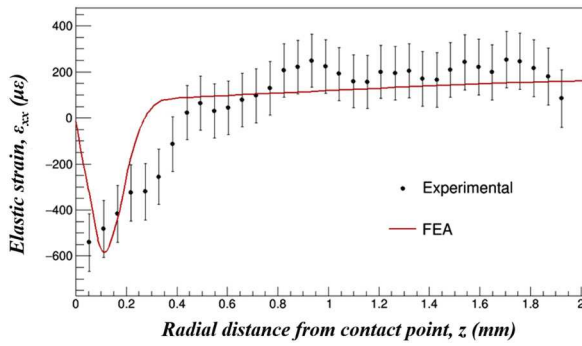
Fig. 10. Subsurface axial (ε_{xx}) strain averaged through the sample, as a function of distance from the contact site, compared to the same component of average FEA strain.

this study demonstrates reasonable correlation between measured elastic strain and those predicted by the model at 10 kN, averaged through thickness the same way that the measurement in the ε_{xx} was carried out. Fig. 10 shows the variation of elastic ε_{xx} strain measured by BEATRIX through the width of the bearing compared with that predicted by finite element simulation. As the distance from the contact site, and highest strain gradients, increases the agreement between the FEA and experiential measurement of elastic strain increases.

Mapping of the Bragg edge broadening parameter, σ, gives an indication of subsurface yielding in bulk engineering components, with a wide range of applications. It may be noted that a detail of the material's manufacturing and post-manufacturing treatment history, if available, could be used to determine microstructural variations, which may influence result accuracy. The active yield area that was generated from FEA corresponds well with the σ maps of the contact area generated by the experiment (see Fig. 11). It was observed that using a threshold σ value of 0.3175 µs, calibrated at 34 kN and then applied to the remaining loads, allowed for reasonable comparisons with predicted plasticity. However, the spatial resolution was not adequate for distinguishing the small elastic region at the contact for 15 kN and 25 kN. There are some discrepancies between experimental data and FEA, notably at 34 kN, where spots above the threshold appear. Without access to repeatable data it is difficult to give an exact explanation, yet it could be speculated that either experimental error or significant microstructural changes at greater loads cause this effect. Whilst an encouraging result, this suggests that future studies will need to be completed in order to quantify plastic strains with Bragg edge imaging, although the σ threshold will vary depending on the sample geometry and material used. For quantitative plastic analysis using energy-dispersive transmission imaging, simpler and well understood sample geometries would be required.

4.2. Future work

Whilst energy-dispersive imaging is a unique method for studying the evolution of subsurface yielding, and Bragg edge broadening is indicative of plasticity, it has yet to be demonstrated as a technique capable of measuring plastic strains quantitatively. Due to the complexity of plastic deformation, and its influence on neutron scattering, the ability to quantitatively study subsurface yielding using such TOF techniques remains a problematic task. Future development of this technique may not only allow for quantitative plastic strain analysis, but also for a more automated approach to FEA and experimental analysis. For instance, it may be possible to develop software capable of cross-correlating experimental data with FEA results to extract the most suitable σ threshold.

Time restrictions for completing this experiment resulted in scan times limited to 2 h per load. Increasing exposure time improves counting statistics, which reduces the size of spatial binning areas, refining the effective spatial resolution. Carrying out the experiment at an
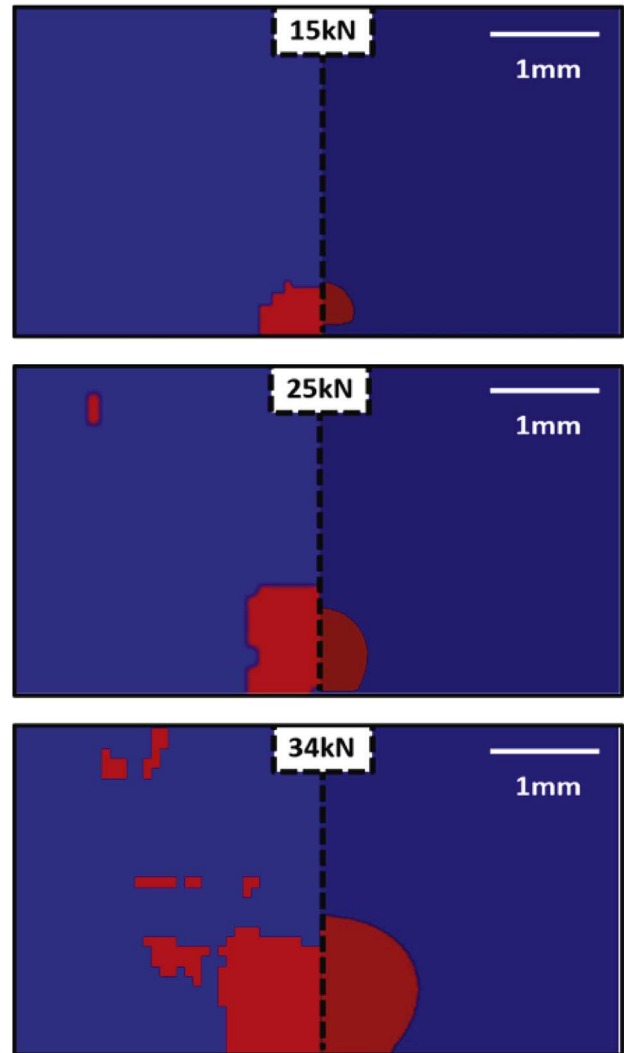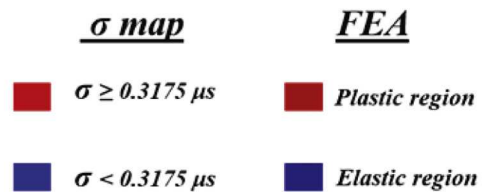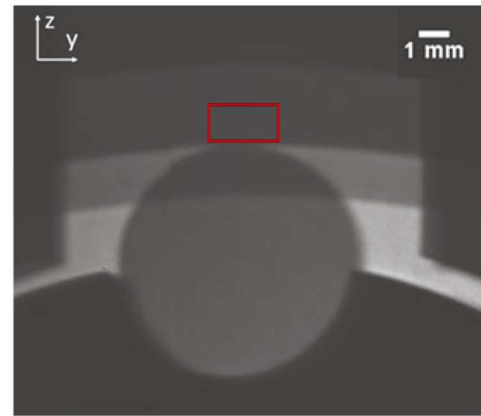

Fig. 11. (Top) Radiograph indicating the region of interest, beneath the contact. (Bottom) Comparison of σ broadening parameter and the active yield region at the contact site, with applied loads of 15 kN, 25 kN and 34 kN load.

imaging beamline, such as IMAT, designed for such high flux experiments ensures that counting statistics are improved. IMAT also uses pin-hole collimator capabilities, allowing for greater control over beam divergence, which is responsible for geometrical blurring effects that can negatively impact spatial resolution. Whilst ENGIN-X has better pulse width (τ parameter), due to using a methane moderator, compared to a hydrogen moderator used at IMAT, this parameter has been fixed for the analysis of results in this. Future studies will use multi-Bragg edge approaches, requiring well-characterised TOF dependencies and correlations between τ and σ parameters, which will lead to gains in spatial accuracy and spatial resolution of mapped parameters.

Fractography results suggest that subsurface yielding may seed defects, impairing bearing performance, yet the tests completed using the FRLF were not fully representative of operational bearing conditions. This experiment will need to be complemented in future work with time-resolved strain measurement in the overloaded region of an in situ dynamic bearing (i.e. a rotary test rig) to give greater confidence that bearing overload events are detrimental to predicted life.

5. Conclusion

- Neutron Bragg edge transmission imaging can be used to visualise the evolution of material yielding non-destructively in bulk engineering components. Quantitative analysis of plastic strains is yet to be demonstrated. It may be possible to determine a σ threshold capable of indicating the presence of plastic deformation in materials of certain sample geometries.

- To gain sufficient counting statistics, long exposure times are required for each scan. Spatial binning techniques may be used to overcome this at the expense of spatial resolution. Alternatively, the use of a dedicated imaging beamline equipped with in situ loading rig, can improve counting statistics.

- Overload events reduce the fatigue life of bearings, with high subsurface shear stresses and the presence of yielding is likely to induce defects that act as a site for crack initiation. Future work on the time-resolved strain in dynamic overloaded bearings, may potentially give greater confidence of the extent of damage caused.

Data availability

Acknowledgements

References

[1] International Organization for Standardization, Wind Turbines–Part 4: Design Requirements for Wind Turbine Gearboxes, ISO/IEC 61400-4: 2012, 2012.

[2] W. Musial, S. Butterfield, B. McNiff, Improving wind turbine gearbox reliability, Eur. Wind Energy Conf 2007, pp. 1–13.

[3] G. Marsh, Offshore reliability, Renew. Energy Focus 13 (3) (2012) 62–65.

[4] R.K. Upadhyay, L.A. Kumaraswamidhas, M.S. Azam, Rolling element bearing failure analysis: a case study, Case Stud. Eng. Fail. Anal. 1 (1) (2013) 15–17.

[5] Z. Ye, L. Wang, Optimization analysis on assembly interference of cylindrical roller bearings, Adv. Mech. Eng. 7 (7) (2015) 1–13.

[6] A. Warhadpande, F. Sadeghi, M.N. Kotzalas, G. Doll, Effects of plasticity on subsurface initiated spalling in rolling contact fatigue, Int. J. Fatigue 36 (1) (2012) 80–95.

[7] A. Bhattacharyya, G. Subhash, N. Arakere, Evolution of subsurface plastic zone due to rolling contact fatigue of M-50 NiL case hardened bearing steel, Int. J. Fatigue 59 (2014) 102–113.

[8] A.S. Pandkar, N. Arakere, G. Subhash, Microstructure-sensitive accumulation of plastic strain due to ratcheting in bearing steels subject to rolling contact fatigue, Int. J. Fatigue 63 (2014) 191–202.

[9] H. Long, R.S. Dwyer-Joyce, T. Bruce, Dynamic modelling of wind turbine gearbox bearing loading during transient events, IET Renew. Power Gener. 9 (7) (2015) 821–830.

[10] N. Weinzapfel, F. Sadeghi, V. Bakolas, An approach for modeling material grain structure in investigations of Hertzian subsurface stresses and rolling contact fatigue, J. Tribol. 132 (4) (2010), 041404.

[11] A. Grabulov, R. Petrov, H.W. Zandbergen, EBSD investigation of the crack initiation and TEM/FIB analyses of the microstructural changes around the cracks formed under rolling contact fatigue (RCF), Int. J. Fatigue 32 (3) (2010) 576–583.

[12] M.H. Evans, White structure flaking (WSF) in wind turbine gearbox bearings: effects of 'butterflies' and white etching cracks (WECs), Mater. Sci. Technol. 28 (1) (2012) 3–22.

[13] A.F. Gourgues, Electron backscatter diffraction and cracking, Mater. Sci. Technol. 18 (2) (2002) 119–133.

[14] M. Kamaya, A.J. Wilkinson, J.M. Titchmarsh, Measurement of plastic strain of polycrystalline material by electron backscatter diffraction, Nucl. Eng. Des. 235 (6) (2005) 713–725.

[15] M.M. Nowell, R.A. Witt, B. True, EBSD sample preparation: techniques, tips, and tricks, Microsc. Microanal. 11 (S02) (2005) 504–506.

[16] A.M. Korsunsky, S.P. Collins, R. Alexander Owen, M.R. Daymond, S. Achtioui, K.E. James, Fast residual stress mapping using energy-dispersive synchrotron X-ray diffraction on station 16.3 at the SRS, J. Synchrotron Radiat. 9 (2) (2002) 77–81.

[17] A. Steuwer, J.R. Santisteban, M. Turski, P.J. Withers, T. Buslaps, High-resolution strain mapping in bulk samples using full-profile analysis of energy dispersive synchrotron X-ray diffraction data, Nucl. Inst. Methods Phys. Res. B 238 (1–4) (2005) 200–204.

[18] M. Mostafavi, et al., Dynamic contact strain measurement by time-resolved stroboscopic energy dispersive synchrotron X-ray diffraction, Strain 53 (2) (2017) 1–13.

[19] P.J. Withers, Fracture mechanics by three-dimensional crack-tip synchrotron X-ray microscopy, Phil. Trans. R. Soc. A 373 (2036) (2015), 20130157.

[20] C. Hammond, The Basics of Crystallography and Diffraction, Fourth ed. Oxford University Press, New York, 2015.

[21] P.J. Withers, P.J. Webster, Neutron and synchrotron X-ray strain scanning, Strain 37 (1) (2001) 19–33.

[22] Z. Budrovic, H. Van Swygenhoven, P. Derlet, S. Van Petegem, B. Schmitt, Plastic deformation with reversible peak broadening in nanocrystalline nickel, Science 304 (5668) (2004) 273–276.

[23] I. Nikitin, M. Besel, Residual stress relaxation of deep-rolled austenitic steel, Scr. Mater. 58 (3) (2008) 239–242.

[24] T. Ungár, J. Gubicza, G. Ribárik, A. Borbély, Crystallite size distribution and dislocation structure determined by diffraction profile analysis: principles and practical application to cubic and hexagonal crystals, J. Appl. Crystallogr. 34 (3) (2001) 298–310.

[25] D. Balzar, H. Ledbetter, Voigt-function modeling in Fourier analysis of size- and strain-broadened X-ray diffraction peaks, J. Appl. Crystallogr. 26 (1) (1993) 97–103.

[26] J.R. Santisteban, M.R. Daymond, J.A. James, L. Edwards, ENGIN-X: a third-generation neutron strain scanner, J. Appl. Crystallogr. 39 (6) (2006) 812–825.

[27] A.J. Allen, M. Hutchings, C.G. Windsor, C. Andreani, Neutron diffraction methods for the study of residual stress fields, Adv. Phys. 34 (4) (1985) 445–473.

[28] A.J. Allen, M.A.M. Bourke, S. Dawes, M.T. Hutchings, P.J. Withers, The analysis of internal strains measured by neutron diffraction in Al/SiC metal matrix composites, Acta Metall. Mater. 40 (9) (1992) 2361–2373.

[29] Y.S. Chen, et al., Direct observation of individual hydrogen atoms at trapping sites in a ferritic steel, Science 355 (6330) (2017) 1196–1199.

[30] Y. Sun, et al., Neutron diffraction studies on lattice strain evolution around a crack-tip during tensile loading and unloading cycles, Scr. Mater. 53 (2005) 971–975.

[31] E.W. Huang, et al., Plastic behavior of a nickel-based alloy under monotonic-tension and low-cycle-fatigue loading, Int. J. Plast. 24 (8) (2008) 1440–1456.

[32] T. Minniti, et al., Materials analysis opportunities on the new neutron imaging facility IMAT@ISIS, J. Instrum. 11 (3) (2016).

[33] M. Connolly, A. Slifka, E. Drexler, In situ neutron transmission Bragg edge measurements of strain fields near fatigue cracks grown in air and in hydrogen, International Hydrogen Conference (IHC 2016): Materials Performance in Hydrogen Environments, 2017.

[34] R. Woracek, et al., Neutron Bragg-edge-imaging for strain mapping under in situ tensile loading, J. Appl. Phys. 109 (9) (2011) 1–5.

[35] T.J. Marrow, et al., In situ measurement of the strains within a mechanically loaded polygranular graphite, Carbon 96 (2016) 285–302.

[36] J.R. Santisteban, L. Edwards, A. Steuwer, P.J. Withers, Time-of-flight neutron transmission diffraction, J. Appl. Crystallogr. 34 (3) (2001) 289–297.

[37] S.R. Agnew, D.W. Brown, C.N. Tomé, Validating a polycrystal model for the elastoplastic response of magnesium alloy AZ31 using in situ neutron diffraction, Acta Mater. 54 (18) (2006) 4841–4852.

[38] Y.B. Guo, C.R. Liu, Mechanical properties of hardened AISI 52100 steel in hard machining processes, J. Manuf. Sci. Eng. 124 (1) (2002) 1–9.

[39] H.K.D.H. Bhadeshia, Steels for bearings, Prog. Mater. Sci. 57 (2) (2012) 268–435.

[40] I. Hutchings, P. Shipway, Tribology: Friction and Wear of Engineering Materials, Butterworth-Heinemann, 2017.

[41] International Organisation for Standardisation, Rolling Bearings - Dynamic Load Ratings and Rating Life, ISO 281:2007, 2007.

[42] T.A. Harris, R.M Barnsby, Life ratings for ball and roller bearings, Proceedings of the Institution of Mechanical Engineers, Part J: Journal of Engineering Tribology 215 (6) (2001) 577–595.

[43] NTN Americas, Cylindrical and Tapered Roller Bearings. Catalog A-1500-III, 2009.
[44] DSS, ABAQUS Analysis User's Manual 6.14-2, DSS (Dassault Systèmes Simulia Corp.), 2014.
[45] ASM International (Ed.), Atlas of Stress-strain Curves, 2nd ed.ASM International, 2002.
[46] K. Shiozawa, L. Lu, S. Ishihara, S-N curve characteristics and subsurface crack initiation behaviour in ultra-long life fatigue of a high carbon-chromium bearing steel, Fatigue Fract. Eng. Mater. Struct. 24 (12) (2001) 781–790.
[47] W. Kockelmann, G. Frei, E.H. Lehmann, P. Vontobel, J.R. Santisteban, Energy-selective Neutron Transmission Imaging at a Pulsed Source, 578, 2007 421–434.
[48] A.S. Tremsin, J.V. Vallerga, J.B. Mcphate, O.H.W. Siegmund, R. Raffanti, High resolution photon counting with MCP-timepix quad parallel readout operating at >1kHz frame rates, IEEE Trans. Nucl. Sci. 60 (2) (2013) 578–585.
[49] A.S. Tremsin, et al., Improved efficiency of high resolution thermal and cold neutron imaging, Nucl. Instrum. Methods Phys. Res., Sect. A 628 (1) (2011) 415–418.
[50] A.S. Tremsin, W.B. Feller, R.G. Downing, Efficiency optimization of microchannel plate (MCP) neutron imaging detectors. I. Square channels with 10B doping, Nucl. Instrum. Methods Phys. Res., Sect. A 539 (1–2) (2005) 278–311.
[51] T. Minniti, Private Communication, 2018.
[52] M.T. Hutchings, P.J. Withers, T.M. Holden, T. Lorentzen, Introduction to the Characterization of Residual Stress by Neutron Diffraction, CRC Press, Boca Raton, FL, 2005.
[53] A.S. Tremsin, J.V. Vallerga, J.B. McPhate, O.H.W. Siegmund, Optimization of Timepix count rate capabilities for the applications with a periodic input signal, J. Instrum. 9 (5) (2014).
[54] A.S. Tremsin, Y. Gao, L.C. Dial, F. Grazzi, T. Shinohara, Investigation of microstructure in additive manufactured Inconel 625 by spatially resolved neutron transmission spectroscopy, Sci. Technol. Adv. Mater. 17 (1) (2016) 324–336.
[55] M.R. Daymond, H.G. Priesmeyer, Elastoplastic deformation of ferritic steel and cementite studied by neutron diffraction and self-consistent modelling, Acta Mater. 50 (6) (2002) 1613–1626.
[56] T.M. Holden, A.P. Clarke, R.A. Holt, Neutron diffraction measurements of intergranular strains in MONEL-400, Metall. Mater. Trans. A 28 (December) (1997) 2565–2576.
[57] T.M. Holden, C.N. Tomé, R.A. Holt, Experimental and theoretical studies of the superposition of intergranular and macroscopic strains in Ni-based industrial alloys, Metall. Mater. Trans. A 29 (12) (1998) 2967–2973.